



Evaluation of an immersed boundary numerical framework to address the wind field in complex urban topographies



Patricia Vanký ^{a,*}, Andreas Mark ^b, Franziska Hunger ^b, Gabriella Villamor Saucedo ^g, Marie Haeger-Eugensson ^{c,g}, Jens Christian Bennetsen ^f, Joaquim Tarraso ^d, Marco Adelfio ^d, Angela Sasic Kalagasisid ^e, Gaetano Sardina ^a

^a Department of Mechanics and Maritime Sciences, Division of Fluid Dynamics, Chalmers University of Technology, Göteborg 412 96, Sweden

^b Fraunhofer-Chalmers Research Centre, Göteborg 412 88, Sweden

^c Department of Earth Sciences, Gothenburg University and COWI, Gothenburg, Sweden

^d Department of Architecture and Civil Engineering, Division of Urban Design and Planning, Chalmers University of Technology, Göteborg 412 96, Sweden

^e Department of Architecture and Civil Engineering, Division of Building Technology, Chalmers University of Technology, Göteborg 412 96, Sweden

^f Center of Excellence for Advanced Simulations, Ramboll, Copenhagen, Denmark

^g COWI AB, Vikingsgatan 3, 41104 Gothenburg, Sweden

ARTICLE INFO

Keywords:

CFD modeling
Experimental validation
Immersed boundary
Street canyon
Urban climate
Wind comfort

ABSTRACT

Estimating the wind velocity field in an urban area is important for pedestrian comfort and safety, as the local wind velocities dictate the transport of heat and air pollution in urban environments. Therefore, it is an essential requirement to assess wind patterns when designing urban areas. Computational Fluid Dynamics (CFD) numerical solvers are usually employed to estimate the wind comfort in an urban area under different wind intensities and directions. However, CFD simulations are expensive in terms of time, especially when many scenarios are addressed to ensure safety and comfort for multiple conditions. Here, a CFD framework based on an immersed boundary approach to discretize the urban topography is developed and validated against experimental data in a wind tunnel and two different standard body-fitted mesh codes. The new solver employs a structured cartesian octree grid automatically generated from Lidar data of urban topographies. The advantages are eliminating the complex and time-consuming pre-processing of urban topographies and making the framework accessible to urban planners without CFD expertise. Furthermore, the code is equipped with GPU parallelization that further reduces the computational time. Provided that the best practice guidelines for urban simulations are satisfied, in particular at least 10 cells between two buildings, the code shows very good agreement in all the tests comprising of a simplified and real urban neighborhood highlighting the importance of accurately solving the complex terrain topography of an urban region when non-negligible elevation changes of the order of 20/40 meters are present.

1. Introduction

In the last decade, global urbanization has made urban areas the most common place of residence. The United Nations is now estimating that by the year 2050, close to 70% of the world's population will be urban residents [1]. At the same time, the cities are developing local microclimates with extreme conditions, which are negatively affecting the local and global environment [2]. The dense building environment, lack of vegetation, and urban areas account for over 70% of CO₂ emissions [3] all affecting the health and liveability of cities. As urbanization does not seem to slow down, we need to improve the ability to plan cities for better urban climate and comfort.

One key factor to consider in urban planning is wind. Wind affects health and lives of urban residents and visitors in many ways, for example, wind comfort, wind safety, and ventilation of street canyons influence the transport of both heat and air pollution [4].

Studying wind in urban areas is done using a combination of statistical meteorological data and aerodynamic information of surrounding buildings and terrain. The final wind conditions can be obtained by either wind tunnel modeling or computational fluid dynamics (CFD), where the latter is becoming increasingly popular [5–12]. There are noticeable advantages to using CFD over wind tunnel testing. Generally, wind tunnel measurements only give data at a limited number of selected points in a region, unlike CFD, which can provide a flow

* Corresponding author.

E-mail address: patricia.vanký@chalmers.se (P. Vanký).

field over large domains. Additionally, CFD simulations easily enable changes in the urban design for assessment.

Despite all advantages of CFD and all studies done on the subject, the CFD assessment in urban planning is typically left until the final stages of a project due to the complexity of the setup of the simulation. At this stage, further strategic interventions are no longer possible. The most common approach to highly detailed urban or neighborhood scale CFD studies is using body-fitted unstructured Cartesian grids [6, 8, 10, 13, 14]. These can be very time-consuming both to generate in the pre-processing of the domain and in terms of simulation time. To help the users in the CFD-setup process, several best practice guidelines (BPG) have been published by Franke et al. [15], Tominaga et al. [16] and Blocken [17]. The BPGs provide information about the necessary accuracy of discretization schemes, the size of the domain, level of details, boundary conditions, turbulence models, and mesh criteria, for example. Moreover, the BPGs suggest Reynolds-Average Navier-Stokes (RANS) model as a mathematical framework to solve the fluid equations of motions, which require turbulence parameterizations for the full range of characteristic scales of the flow allowing large time steps and steady-state simulations. A more computational expensive, but more accurate, framework is Large-Eddy Simulation (LES), a technique that explicitly solves the large energy-containing scales of the flow and model just the smaller scales. Therefore, LES is less reliant on turbulence models and gives instantaneous information in time on the flow field, capturing unsteady phenomena more effectively, but at a price of more computational resources. LES simulations are nowadays mature for urban simulations [18, 19], but they are still limited to the scientific research environment. Almost all practitioners still employ RANS models, and for this reason, we will focus just on this numerical approach in this work.

Although the BPGs are intended to guide users, they do not constrain the complexity of the setup required to meet these criteria. Therefore, there is a need to develop new numerical methodologies that offer a simpler setup process without compromising accuracy. Simplifying the setup is essential to encourage urban planners to use these tools early in the design process, as it reduces the time required to try out different designs.

One approach to limit the complexity of setting up urban simulations would be to ease the meshing process. The mesh generation is computationally intensive [20] and can take a substantial amount of time in the entire simulation process. For example, Kim [21] reports that the time for efficiently generating a high-resolution mesh for the urban CFD analysis in their study was 80% of the total simulation time. Therefore, the meshes should be generated within a considerable time since the total runtime is a critical factor for evaluating the efficiency of simulations. Here, we describe and validate a numerical solver based on an immersed boundary method (IBM) which eliminates the need for body-fitted meshes as the urban boundaries are represented by introducing body forces in the cells, which then allows for easily generated structured grids [22]. There are a few papers published on the use of immersed boundary techniques for urban scale simulations [23–27] which handle both idealized and relative simple city models as well as actual urban models, however none of the published work considers a complex ground topography. There are also papers considering immersed boundary over complex terrain [28] but without the presence of other urban solids like buildings.

Another strategy to integrate urban simulations into early stages of urban design is to increase their accessibility. While common CFD codes are usually highly parallelizable on the CPU, true benefit can only be gained when computer clusters are available that allow computations over many nodes and large numbers of CPUs. Here, the computational time can significantly be decreased using more CPUs but depends on the scalability of the CFD code. The framework introduced in this work utilizes the GPU in addition to the available CPUs which makes such simulations suitable for a desktop computer effectively using its hardware components or a single node on a computing cluster.

This paper validates a user-friendly fluid dynamic numerical solver based on the Reynolds Averaged Navier–Stokes (RANS) and the immersed boundary methodology is validated against wind tunnel data from Allegrini [29]. Furthermore, the wind field is evaluated over a complex ground and urban topography in Gothenburg, Sweden, compared to the results of two other CFD codes commercially used by industry. The numerical framework in question employs an automatic generation of a Cartesian octree grid, eliminating the complex pre-processing of urban topographies, promoting ease of use, and making the framework accessible for general users with different backgrounds.

2. Methodology

There are many CFD approaches used for simulations of urban flow and there are advantages and disadvantages with all of them. Here steady-state RANS is used due to its computational speed, but also because it has commonly been used for urban CFD simulations. The best practice guidelines suggest using the $k-\epsilon$ to model the turbulence for efficient computation; however, there is limited evidences of the performances of other turbulence models in urban simulations. Less common in urban wind simulations is the use of the immersed boundary method, which allows for modeling the complex urban topography without an unstructured body-fitted mesh.

2.1. Flow solver

The flow solver used in this paper is an in-house code developed at Fraunhofer-Chalmers Research Center called IBOFlow® [30]. As mentioned the solver employs steady-state Reynolds' averaged Navier–Stokes equations,

$$\nabla \cdot \vec{u} = 0, \quad (1)$$

$$\frac{\partial \vec{u}}{\partial t} + \vec{u} \cdot \nabla \vec{u} = -\frac{\nabla p}{\rho} + \nabla \cdot ((v + v_t) \nabla \vec{u}), \quad (2)$$

along with the turbulent transport equations. In the above equations, \vec{u} represents the mean velocity field, ρ the air density, p the mean pressure, v and v_t are the molecular and turbulent kinematic viscosities.

The equations are discretized using the finite volume methodology on a Cartesian octree grid, with the convective terms approximated using the first-order upwind scheme and the diffusive terms using the central difference scheme. An adapted grid refinement algorithm automatically increases the resolution close to the ground and the buildings or at specific regions defined by the user. The RANS equations are solved in a segregated manner, and pressure and velocity fields are coupled using the SIMPLEC method [31]. All variables are stored in a co-located arrangement, and pressure oscillations are suppressed with a weighted flux interpolation [32]. The steady state solver uses artificial time stepping and the equations are solved until all relative solution residuals are lower than a given threshold, or oscillatory convergence is reached [17].

The numerical framework has several convective schemes implemented, including higher-order schemes. A test has been conducted using second-order upwind and ultimate quickest, to ensure that the accuracy of the simulation is maintained. This verification step confirms that even with a first order convective scheme, the results remain reliable and precise.

Finally, the code employs the mirroring immersed boundary method [33] to account for the presence of all geometries in a Cartesian grid, avoiding a body-fitted mesh. The input geometries consist of an oriented triangulated surface mesh automatically connected to the background grid describing the local topography of the terrain and the buildings. The Cartesian grid inherently handles self-intersecting surfaces of the input geometries without requiring modifications, unlike traditional meshing techniques which struggles with these complexities. During this process, cells are classified as interior, fluid, or boundary cells based on the position of the input geometries. To

address potential issues with fluid cells being located inside buildings, a post-correction step is implemented, ensuring that all fluid cells are connected to the z-top boundary, representing the sky. Cells that lack this connection are reclassified as interior cells. This approach also ensures that too narrow channels or street canyons are appropriately closed, always assuring a stable solution. This renders the solver highly effective for utilizing automated meshing, without the need for time-consuming pre-processing of the surface meshes.

2.2. Turbulence models

Three turbulence models are employed and compared in this paper, the Spalart–Allmaras, the realizable $k-\epsilon$ and the $k-g$ SST model which is based on the $k-\omega$ SST model.

In the Spalart–Allmaras model the kinematic turbulent eddy viscosity is evolved. The kinematic turbulent eddy viscosity is given by $\nu_t = f_{v1}\tilde{v}$, where the viscous damping is given by $f_{vt} = \frac{\chi^3}{\chi^3 + c_{v1}^3}$, where $\chi = \frac{\tilde{v}}{v}$. Further, \tilde{v} is given by

$$\frac{\partial \tilde{v}}{\partial t} + \vec{u} \cdot \nabla \tilde{v} = P - D + \frac{1}{\sigma} [\nabla \cdot ((v + \tilde{v}) \nabla \tilde{v}) + c_{b2} |\nabla \tilde{v}|^2], \quad (3)$$

with P being the production term and D is the destruction term. A complete description of the model can be found in [34]. When using the immersed boundary method, \tilde{v} is set to zero on the geometries by an implicit immersed boundary condition. The Spalart–Allmaras turbulence model is simple and effective, however lacks in handling complex, separated, and transitional flows [35]. However, in urban regions where large parts of the domain are wall-bounded and the turbulence is fully developed, it can be quite effective for a limited computational cost.

The advantage of using the realizable $k-\epsilon$ model [36] over the Spalart–Allmaras model due to its ability to handle complex flow phenomena. It is better at predicting flows with significant separation, recirculation, and free shear layers [35], which are common in urban environments with buildings and varying terrain. The model may fall short in accurately resolving near-wall effects, transitional flows, highly anisotropic turbulence. The benefit of using the realizable $k-\epsilon$ model instead of the standard model is that it solves issues with rotating flows. Here, S_{ij} is defined as the mean strain and Ω_{ij} as the rotation rate tensor, the governing equations for the model are then

$$\frac{\partial k}{\partial t} + \vec{u} \cdot \nabla k = \nabla \cdot \left(\left(v + \frac{\nu_t}{\sigma_k} \right) \nabla k \right) + \nu_t S^2 - \epsilon, \quad (4)$$

$$\frac{\partial \epsilon}{\partial t} + \vec{u} \cdot \nabla \epsilon = \nabla \cdot \left(\left(v + \frac{\nu_t}{\sigma_k} \right) \nabla \epsilon \right) + C_{1\epsilon} S - C_{2\epsilon} \frac{\epsilon^2}{k + \sqrt{\nu \epsilon}}, \quad (5)$$

$$\nu_t = C_\mu \frac{k^2}{\epsilon}, \quad (6)$$

where $S = \sqrt{2S_{ij}S_{ij}}$, $C_{1\epsilon} = \max(0.43, \frac{\eta}{\eta+5})$ and $\eta = S \frac{k}{\epsilon}$. Note that the eddy viscosity coefficient changes as

$$C_\mu = \frac{1}{A_0 + A_s \frac{kU^*}{\epsilon}}, \quad (7)$$

where $U^* = \sqrt{S_{ij}S_{ij} + \Omega_{ij}\Omega_{ij}}$, $A_0 = 4.04$, $A_s = \sqrt{6\cos\phi}$, $\phi = 1/3 \arccos \sqrt{6}W$, and $W = \frac{S_{ij}S_{jk}S_{ki}}{\sqrt{(S_{ij}S_{ij})^3}}$.

As mentioned, the $k-g$ SST model is based on the $k-\omega$ SST model where the turbulence is modeled by the Menter SST (shear-stress transport) [37,38] model that considers both the standard $k-\epsilon$ model, and the original Wilcox $k-\omega$ equation [39],

$$\frac{\partial k}{\partial t} + \vec{u} \cdot \nabla k = P - \beta^* \omega k + \nabla \cdot ((v + \sigma_k \nu_t) \nabla k), \quad (8)$$

$$\begin{aligned} \frac{\partial \omega}{\partial t} + \vec{u} \cdot \nabla \omega &= \frac{\gamma}{\nu_t} P - \beta \omega^2 + \nabla \cdot ((v + \sigma_k \nu_t) \nabla \omega) \\ &+ 2(1 - F_1)\sigma_\omega \frac{1}{\omega} \nabla k \cdot \nabla \omega, \end{aligned} \quad (9)$$

$$\nu_t = \frac{a_1 k}{\max(a_1 \omega, F_2 S)}. \quad (10)$$

The hybrid method switches between $k-\omega$ close to walls by setting $F_1 = 1$ and $k-\epsilon$ in the free-stream ($F_1 = 0$). The strain rate and the damping factor F_2 , which is 1 at walls, is used for damping the eddy viscosity. In an immersed boundary setting the SST model has to be adapted by changing the variable ω to the turbulence time scale $g^2 = \frac{1}{C_\mu \omega}$, for more details see [40]. Both k and g are set by wall functions at the boundary of the geometries with the immersed boundary method. This blending of the different models makes the $k-g$ SST model provide accurate near-wall treatment and handle adverse pressure gradients well [35].

2.2.1. Boundary conditions

For the simulations, the domain boundary along the lowest x-coordinate is set as a velocity inlet. The inlet air velocity profile used in the case study, $u(z)$, the turbulent kinetic energy, $k(z)$ and turbulence dissipation rate, $\epsilon(z)$ are formulated as by Richards and Hoxey [41] presented in Eqs. (11)–(13).

$$u = \frac{u^*}{\kappa} \ln \left(\frac{z + z_0}{z_0} \right), \quad (11)$$

where κ is the von Karman constant = 0.42 and u^* is the friction velocity defined in Eq. (14).

$$k = \frac{u^*}{\sqrt{C_\mu}}, \quad (12)$$

where C_μ is a constant = 0.09.

$$\epsilon = \frac{u^*}{\kappa(z + z_0)}, \quad (13)$$

The atmospheric boundary layer friction velocity can be defined through a reference velocity, u_{ref} , at a reference height, h_{ref} .

$$u^* = \frac{\kappa u_{ref}}{\ln \left(\frac{h_{ref} + z_0}{z_0} \right)}, \quad (14)$$

The z-coordinate is defined as 0 at the ground height for each cell, and the reference height is set to 10 m above the ground level, as this is the height of the weather station where all wind conditions are measured. The reference velocity was set to 5 m/s. The surface roughness, z_0 , was set to 0.5 to account for the low-rise dense buildings at the inlet location, according to definitions of [42].

In the case of the experiment validation, the inlet velocity profile was defined using the wind profile power law

$$u = u_{ref} \left(\frac{z}{z_{ref}} \right)^n \quad (15)$$

with $n = 0.38$ as defined in [29] based on the measured velocity. The measured turbulence intensity at the inlet is also given for the experiment.

The outlet is set as an open pressure outlet where the dynamic pressure is added to the static pressure at the outlet. The other lateral domain boundaries, as well as the top boundary, are set as symmetry boundaries.

The boundary conditions of the geometries within the domain are defined as implicit immersed boundary conditions. The solver used in this paper employs a unique mirroring immersed boundary method described in detail in [30,33]. In short, the centers of mirroring cells that lie close to the fluid surface are geometrically mirrored over the immersed boundary to the centers of the exterior cells. This mirroring ensures a second-order accurate solution of the velocity field.

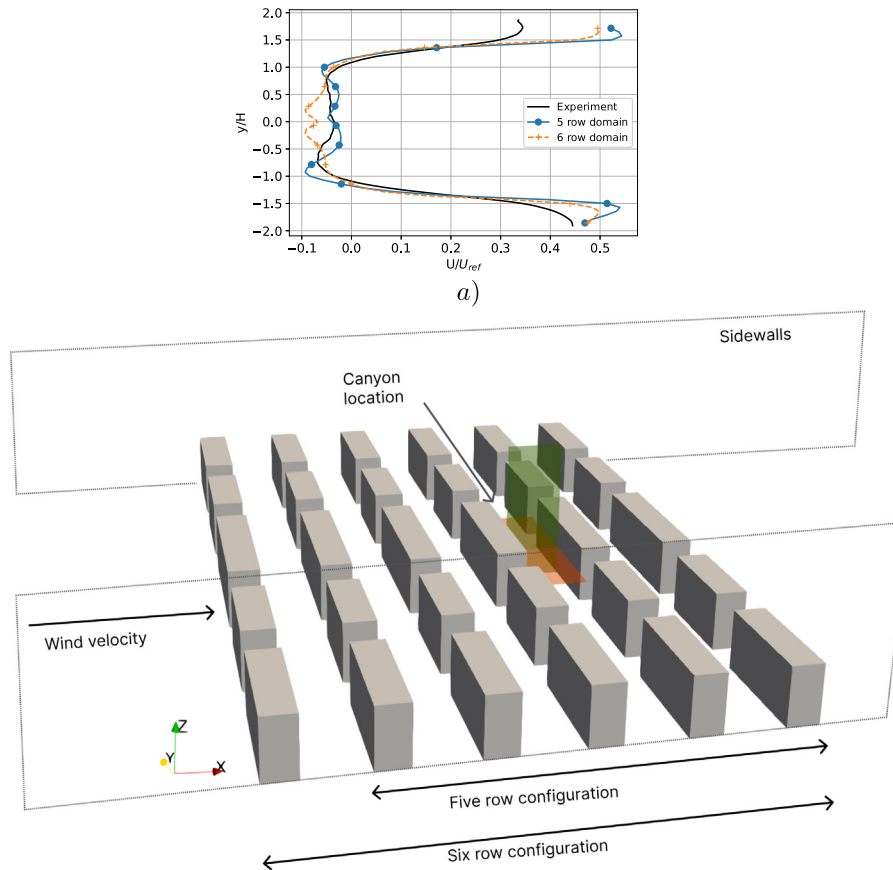


Fig. 1. (a) Velocity profiles of the horizontal average velocity component at the center of the street canyon for case A. The simulation results in different domain configurations (solid lines with symbols) are compared against PIV experimental data (solid black lines). (b) 3D visualization of the domain where the red and green planes show the horizontal (at half flat roof height) and vertical PIV planes, respectively. The flow direction is in positive x-direction. (For interpretation of the references to color in this figure legend, the reader is referred to the web version of this article.)

2.2.2. Wall functions

For high Reynolds number flows, where the first grid point lies outside the viscous sub-layer, wall functions are used to estimate the stresses on the ground and the buildings. In this work, the cells inside the fluid but close to the surface are identified and for each such cell, universal wall functions from Spalding [43] are used to calculate the local fluid stress and the dissipation rate at the wall. This is done one cell size away from the immersed boundary in the normal direction. As this point typically does not coincide with the cell centers, the required fluid properties are interpolated to the point. The stress is then applied on the local wall by an explicit force and the dissipation rate is set by a Dirichlet immersed boundary condition. The turbulent kinetic energy boundary condition is treated with an implicit zero gradient immersed boundary condition. For the Spalart-Allmaras model the kinematic turbulent viscosity is set to zero at the wall by an implicit immersed boundary conditions. This can be done as it decays linearly close to the wall.

Furthermore, to include roughness contributions in regions where larger obstacles, such as buildings, are not explicitly modeled, surface roughness parameters are used in terms of wall functions. The momentum and the different turbulence models have different modifications or wall shifts [44–46]. Implicit modeling of roughness in atmospheric boundary layers is typically expressed by the introduction of an aerodynamic roughness length z_0 [42,47]. However, most numerical tools, including the one used in this paper, express non-explicitly modeled roughness as wall functions where the roughness is expressed in terms of a sand grain roughness height k_s [48]. For atmospheric boundary

layers, the relation between the Davenport-Wieringa roughness length, z_0 , and the sand grain height, k_s can be defined as $k_s = 30z_0$ [48].

3. Validation

The described numerical framework is validated against Particle Image Velocimetry (PIV) experimental data by Allegri [29]. The experiments are performed over a compilation of wooden blocks of various sizes that are placed in a wind tunnel to describe an idealized urban area. A complete simulation of the wind tunnel experiment with all the buildings requires laborious work and is believed to be unnecessary to achieve fully developed turbulence at the area of interest. Therefore, the simulations were performed over a portion of the domain, including only the central, structured part of the simplified urban area. Two configuration variations of the CFD-domain were tested for an inlet velocity, U_{ref} , of 1.94 m/s and compared against the laboratory measurements to find the minimum domain size that gives reasonable results. The first domain configuration consists of the 5×5 rows of structured houses, whereas the second configuration has the same set-up but with an additional sixth row added upstream to develop the flow further. Both domains include a developing region upstream of the buildings of approximately four times the building height, H .

The horizontal velocity profile was the most sensitive quantity that was changing in the two configurations, and these variations are presented in Fig. 1a. As can be seen, both domains give similar results, but with the six rows we capture more of the upstream effects. Therefore, the six-row domain was used for all the following simulations.

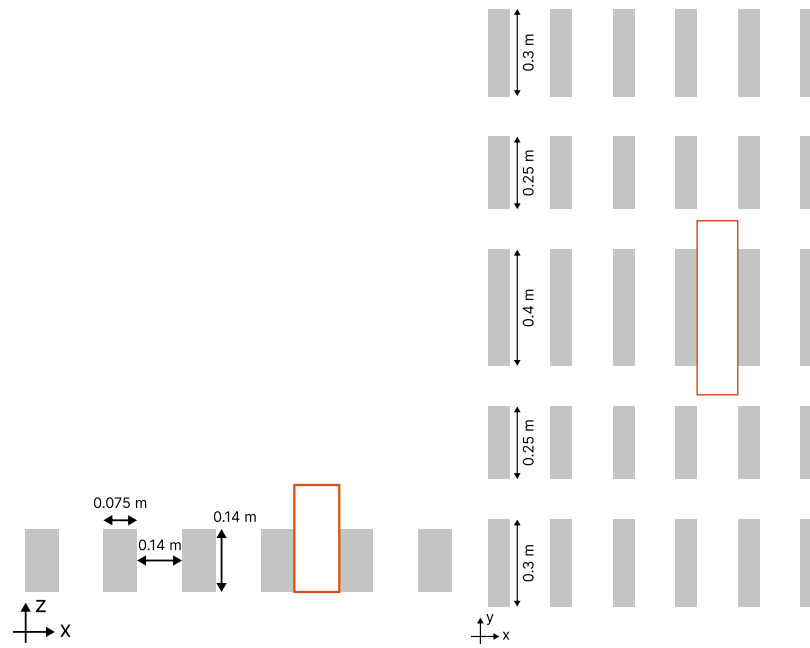


Fig. 2. Side (left panel) and top (right panel) views of the geometrical configurations of the investigated case. The area marked in red represents the position of the canyon where the PIV planes are located. (For interpretation of the references to color in this figure legend, the reader is referred to the web version of this article.)

The domain configuration can be viewed in Fig. 1b, where the PIV-measurement planes are marked in red (horizontal) and green (vertical). The vertical plane is located at the center of the canyon, and the horizontal plane is set at half of the flat roof height.

In the simulated domain, the houses are varying in dimension across different columns. The flat roof height, H , and building depth remain consistent for all houses, measuring 0.14 m and 0.075 m, respectively, while the width varies. The first and last columns consists of buildings with a width of 0.3 m and the houses in the second and fourth columns are 0.25 m in width. The middle column has varying configuration depending on the case; In this case we consider case A which has all flat roof buildings and no variation of building width within the column as shown in Fig. 2. The total simulation domain, together with a developing region, is of the size $2.0 \times 1.9 \times 0.85$ m.

The grid of the simulation domain is set up with a uniform base cell size of $0.05 \times 0.05 \times 0.05$ m, which is refined around the near-wall regions of the ground and buildings. The ground and buildings along the sides of the domain are refined two times, whereas the six buildings along the middle column, where the measurements were taken in the experiment, is refined further, up to four additional refinements corresponding to 48 grid points inside the canyon and a total of approximately four million cells in the domain. A grid study to find the number of refinements to reach numerical convergence of the mean velocity field will be described in the next section. We will then validate our numerical framework against the wind tunnel experimental data.

3.1. Grid convergence study

The uniform base cells of the domain are refined twice close to all the buildings and the ground surface; in addition, the cells in the region where the measurements were taken in the experiments are refined further, up to four times. Two, three and four refinement levels represent 12, 24 and 48 grid points over the width of the canyon, respectively. Comparisons of the results with the variation of refinements in this region, simulated using k-g SST turbulence model, are shown Figs. 3–5 together with the visualization of the geometrical mesh in the vertical and horizontal plane to better appreciate the cell distribution. A qualitative evaluation of the average velocity magnitude contours in

Figs. 3 (vertical plane) and 4 (horizontal plane) show reasonable agreement with the experimental data for all three simulation grids. A more quantitative comparison is presented in Fig. 5, where the (a) vertical and (b) horizontal profiles of the horizontal mean velocity component are shown. The velocity profiles indicates some differences between the grids, but the differences are small, averaging a 0.02 difference in the normalized velocity. A grid refinement of four in the canyon is used for all the following simulations. It is worth noting that 48 grid points in the canyon will be too computationally expensive for the simulations of a real urban region. For these cases, even two refinements or 12 grid points per canyon could still give reasonable performance in estimating the order of magnitude of the wind according to these results. This aligns well with the BPGs presented in Section 4.1, which suggest 10 cells between

3.2. Comparisons between turbulence models

In addition to comparing the results using varying domains and grid resolution, a sensitivity study of three different turbulence models has been performed on the domain with six rows of housing and a grid resolution of four in the measurement region. These results are displayed in Figs. 6 and 7.

Fig. 6 shows that while there is a discrepancy in the vortex location between the experimental and simulated results, the velocity magnitude and overall flow direction are mainly consistent. The error plots show that the most significant deviations, up to an error of 0.35 in the normalized measured velocity, occur in the near-wall regions, particularly at the corner where the flow enters the canyon. In the center of the canyon, all simulations show results that are close to the experimental measurements. In the center of the canyon, all simulations are showing results close to the experimental measurements. Fig. 7 shows a closer look at the velocity comparison along the center of the canyon, all three turbulence models give results close to the experiments both along the vertical (left panel) and horizontal (right panel) plane, within the margin of error for the measurements. There are some discrepancies in the near-ground area; however, the overall results are satisfactory. The horizontal velocity profile show that in the canyon perpendicular to the flow, the one-dimensional velocities are similar to laboratory-measured results, although the vortex centers are not in the same position.

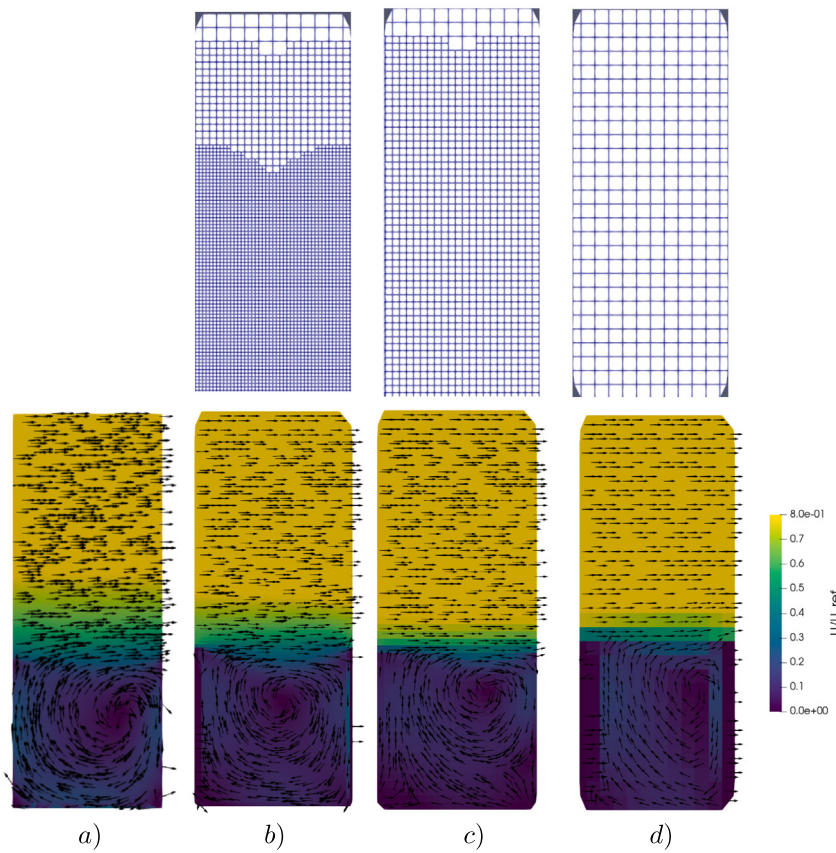


Fig. 3. Contour plots and streamlines of the in-plane average velocity magnitude on the vertical plane. The panels represent the (a) PIV data followed by the results of three simulations with different grid resolutions, (b) 4 refinements, (c) 3 refinements, and (d) 2 refinements. The top panels show the cell distribution in the vertical plane depending on the refinement level.

4. Case study: Urban neighborhood in the city of Gothenburg

After validating with experimental data, we simulate the wind field in an urban neighborhood in Gothenburg. To assess the quality of the results, we compare our data with two body-fitted solvers already established in the field of urban simulations: MISKAM and Helyx.

The comparison is made around Arena Staden and the Gårdaberg area in Gothenburg, Sweden. The focus region is approximately 1.8 km^2 in size and is located in the valley at a reference altitude of around 40 m above the sea between two inclinations. The results are collected on an area of around $800 \times 1000 \text{ m}^2$, an elevation map (relative to the reference altitude) of this region can be seen in Fig. 8b showing the complex rough morphology of the terrain. The largest elevation difference in the simulation domain is of the same order as the tallest building, in the area of interest this ratio is 0.5. This would indicate that the terrain will have significant impact on both the wind flow paths in the region as well as local wind velocities. For better quantitative comparisons, one-dimensional data containing the modulus of the wind velocity have been collected at the black solid lines indicated in Fig. 8a at two different local height: 1.5 m corresponding to pedestrian level and 10 m. The neighborhood includes both a highway (on the right of 8a) and other high-traffic roads as well as dense residential and commercial areas and is surrounded by complex structures such as dense urban regions, green areas and a water stream. All the simulations included in this case study assume a turbulent inlet profile of wind velocity coming from South direction and with intensity of 5 m/s at 10 m high.

4.1. Computational domain

The computational domain consists of three different levels of geometrical modeling. In the central region, both the buildings and

topography are explicitly modeled based on Light Detection and Ranging (LiDAR) data and property maps provided by Lantmäteriet [49] which were used to generate a triangulated surface mesh using DTCC Builder [50] as described in [51]. Surrounding this explicitly modeled region is a region which explicitly models the topography but implicitly models the buildings by assigning a sand grain roughness, k_s , to the ground as described in Section 2.2.2. Finally, within the explicitly modeled region is a smaller region where the results are extracted. The sizing of these different regions is based on the BPGs, which suggest that the distance from the inlet and lateral boundaries to the explicitly modeled buildings should exceed the length $5H_{max}$, where H_{max} is the height of the tallest building. In the same way, the distance to the outlet boundary should be approximately $10H_{max}$ to allow for full wake flow development. Further, the blockage ratio of the domain, $BR = A_{buildings}/A_{domain}$, should not exceed 3%. To fulfill these guidelines, domain size was set to $4300 \times 4000 \times 520 \text{ m}^3$. A geometrical representation of the domain can be viewed in Fig. 8b where the different colored regions represent the modeling approaches.

Regarding the computational grid, the BPGs consider only prismatic cell body-fitted meshes, which are not used with this immersed boundary approach where an octree grid automatically refined along the geometries is employed. However, the BPGs are followed where applicable.

We perform a grid convergence study discussed in Section 4.2. The chosen grid for the remaining study is named G6 and described in the following. We utilize a base grid of size $60 \times 56 \times 11$ cells with six cell refinements around the buildings and the ground in the explicitly modeled part, and three refinements at the ground in the implicitly modeled region. This results in skewed cells of a minimum cell size near the buildings and the ground of approximately $1 \times 1 \times 0.73 \text{ m}^3$.

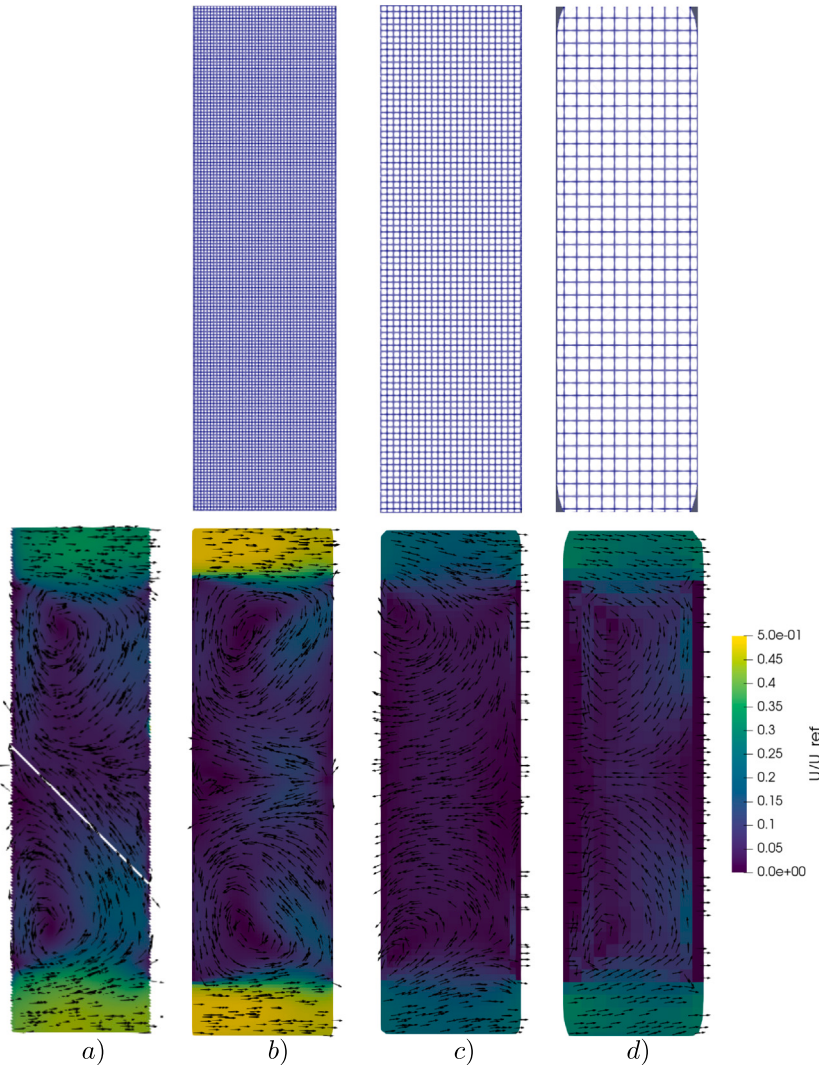


Fig. 4. Contour plots and streamlines of the in-plane average velocity magnitude on the horizontal plane at half flat roof height. The panels represent the (a) PIV data followed by the results of three simulations with different grid resolutions, (b) 4 refinements, (c) 3 refinements, and (d) 2 refinements. The top panels show the cell distribution in the horizontal plane depending on the refinement level.

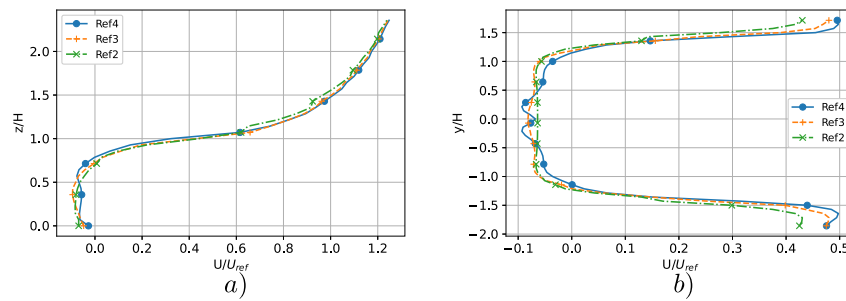


Fig. 5. (a) Vertical and (b) horizontal profiles of the horizontal average velocity component at the center of the street canyon for case A. The numerical results at different grid resolutions.

With this setting, most street canyons are locally resolved with 10 cells and the pedestrian height 1.5 m lies in the third cell layer.

In total, IBOFlow employs approximately 18.5 million cells for the entire domain, with the majority of cells located close to the ground

in the region with explicitly modeled buildings. This is the mesh resolution that was automatically achieved without taking special care to, for example, narrow streets. The time devoted to mesh generation can be disregarded in relation to the simulation time.

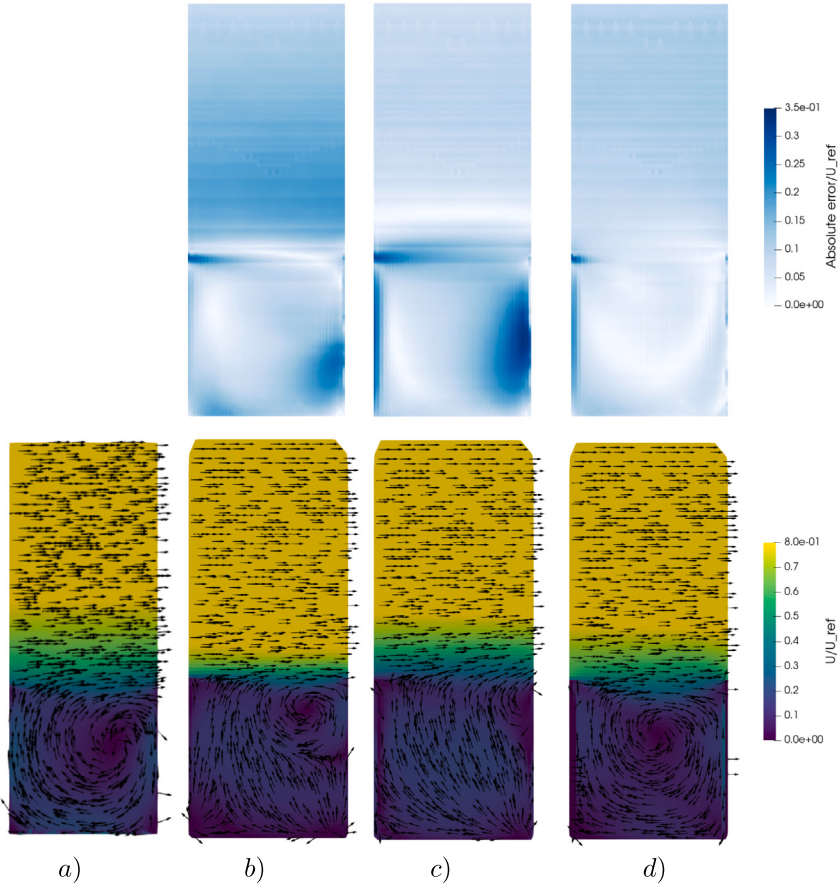


Fig. 6. Contour plots and streamlines of the in-plane average velocity magnitude on the vertical plane for different turbulence models: (a) Reference experimental results, (b) k-g SST model, (c) Spalart-Allmaras model, (d) k- ϵ model. The top panels show the normalized error between the simulated results and the experiment data.

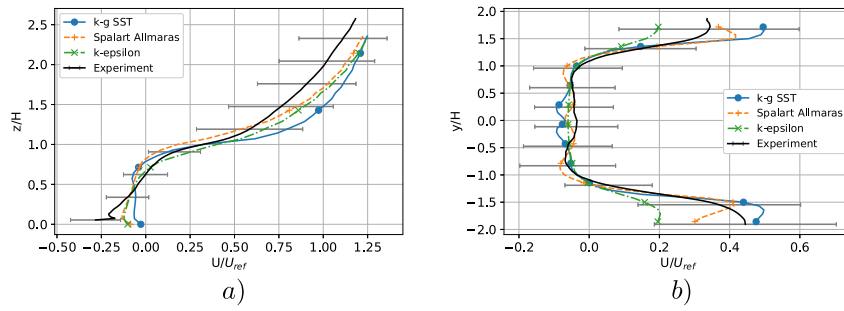


Fig. 7. (a) Vertical and (b) horizontal profiles of the horizontal average velocity component at the center of the street canyon for case A. The numerical results with different turbulence models (colored lines with symbols) are compared against PIV experimental data (solid black line) and the standard deviation of the measurements. (For interpretation of the references to color in this figure legend, the reader is referred to the web version of this article.)

Table 1
Performance comparison of the grids.

	Grid 4	Grid 5	Grid 6	Grid 6.5
No. Cells	1.6 Mio	4.8 Mio	18.5 Mio	36.0 Mio
RAM [GB]	13	19	44	60
GPU memory [GB]	2	3	8	14
Wall clock time scaled to usage of 12 CPUs for 3000 iterations [h]	0.8	2.5	10.5	34

4.2. Grid convergence study

We evaluate the convergence of the predicted velocity to grid refinement in this real urban neighborhood similarly as performed in

the wind tunnel case, see Section 3.1. An extract of the meshes with different grid refinement level is shown in Fig. 9. The figure shows the cell distribution in a typical street canyon of the computational domain, highlighting the grid refinement clusters close to each building and at the ground. In particular, the four cases are characterized by a different total number of cells. Along a typical street canyon the grid with the four refinement levels contains 4 cells (panel a) at the middle height of the canyon, the grid with five refinements has 6 cells (panel b) and finally, the grid with six and six and a half refinements have 11 cells (panel c and d). The extra refinement in the finest mesh is achieved by decreasing the overall base cell size. The last two refinement levels are in agreement with the BPGs suggesting at least 10 cells between two buildings. Clearly, the cases with higher refinements have more points located close to the building walls and at the ground. Different

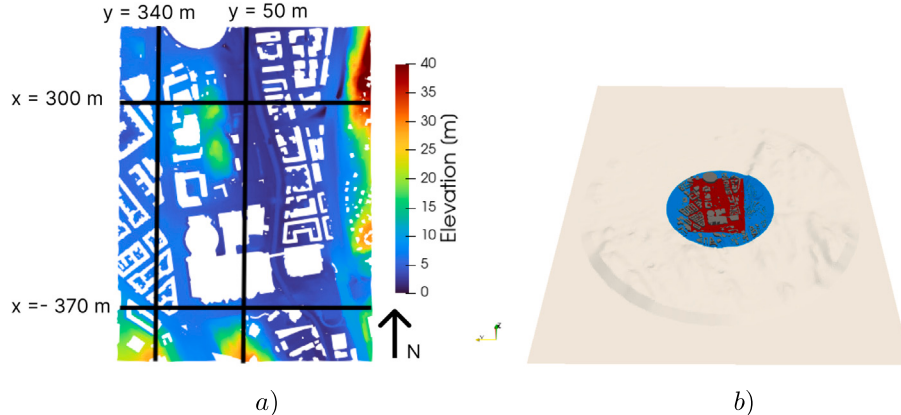


Fig. 8. (a) Relative elevation in meters over the simulated domain of the study case. The black solid lines indicate the extraction location of the wind velocity magnitude to generate one-dimensional comparisons. (b) Computational domain ($4300 \times 4000 \times 520 \text{ m}^3$) viewed from the south. In the blue region, the buildings are explicitly modeled, the gray region is implicitly modeled, and the red region is where the results are collected. (For interpretation of the references to color in this figure legend, the reader is referred to the web version of this article.)

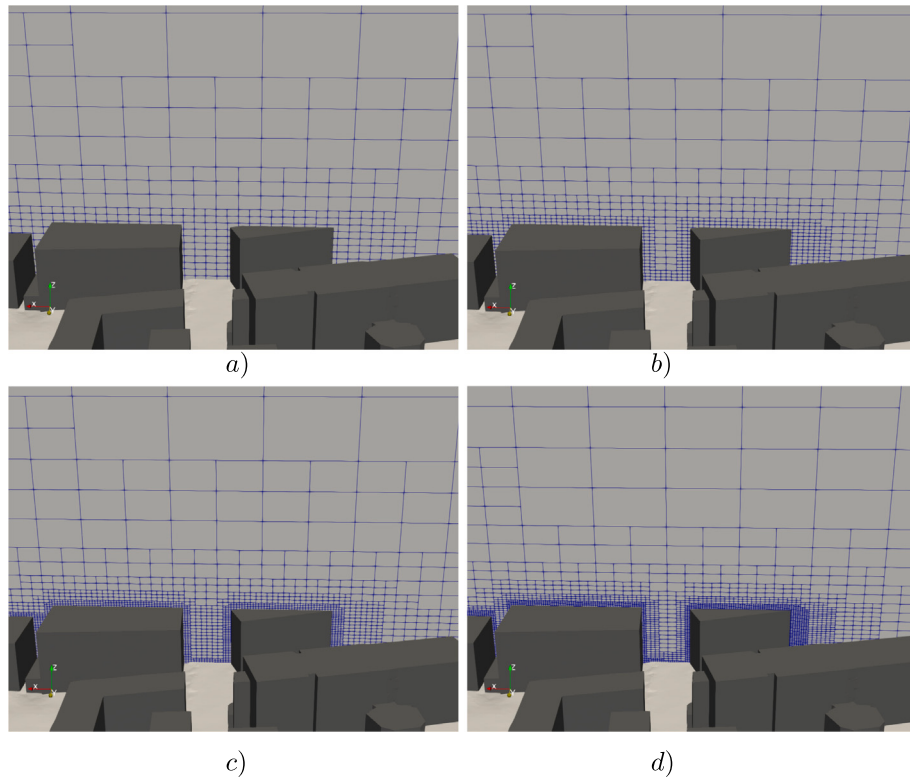


Fig. 9. Mesh details inside a typical street canyon of the area under investigation: (a) four refinement levels, (b) five refinement levels, (c) six refinement levels, (d) six and half refinement levels.

grids obtain different computational performances which are compared in Table 1. The simulations for the grid-convergence assessment has been run using a $k-g$ SST model. Our convergence tests using different turbulence models indicate the same trend.

Fig. 10a-d shows the wind velocity magnitude for the four resolution cases at a height of 1.5 m above the local ground level, corresponding to the wind perceived by pedestrian. We observe lower values of the wind velocity in the numerical solutions with the coarsest grid (panel a)) compared with the larger refinement grids (panels b), c) and d)). The reason is probably due to the numerical diffusion that smooths the velocity in the coarser cells. In particular, the coarser cases cannot sufficiently resolve the higher velocity peaks of the finer refinement levels at the center of the computational domain and in the front of the larger building in the bottom part of the neighborhood.

Less differences between the four cases emerge at a local height of 10 m as plotted in Fig. 10e-h. This region is far from the ground so the gradients of wind velocity are less steep compared to the 1.5 m and they can be sufficiently resolved also from the coarser mesh. The solution looks similar in the four cases, again, showing slightly larger wind intensities compared with the other two coarser grids.

A more quantitative evaluation of the effects of grid refinement is shown in Fig. 11 where the wind velocity magnitude is extracted along the vertical and horizontal lines specified in Fig. 8 at 1.5 m. The qualitative impression observed in the contours plots is confirmed by the line plots. In particular, the grid with four refinement levels consistently under-predicts the wind velocity, as expected.

Regarding the three finest resolutions, we observe just minimum differences in the points with maximum velocity magnitudes in both

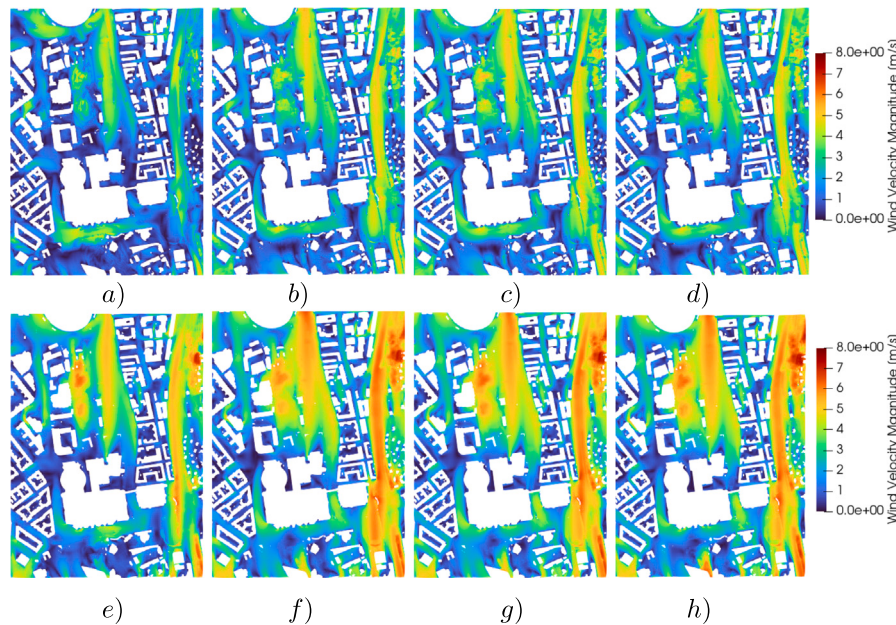


Fig. 10. Wind velocity magnitude at different refinement level over a plane 1.5 m (panel a-d) and 10 m (panels e-h) above ground level: (a) and (e) four refinement levels, (b) and (f) five refinement levels, (c) and (g) six refinement levels, (d) and (h) six and a half refinement levels.

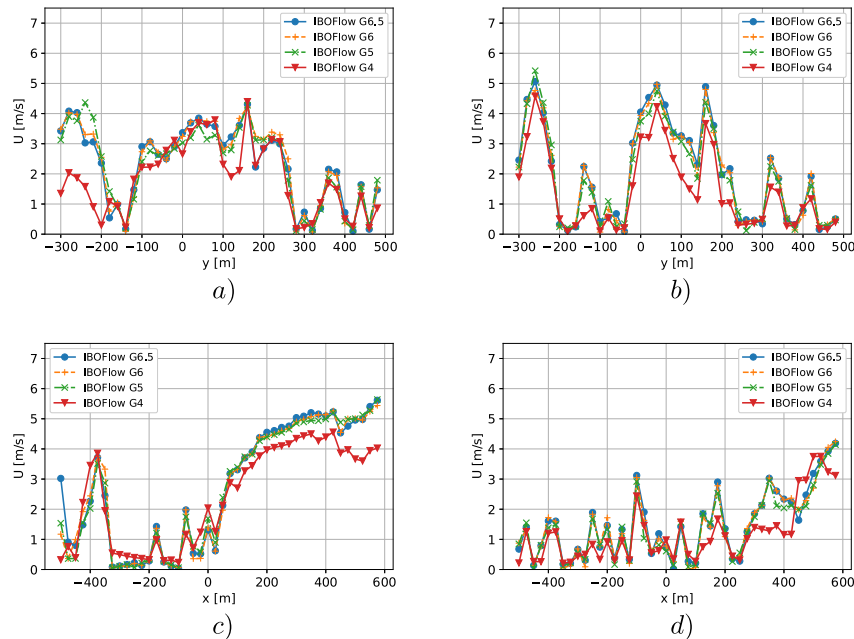


Fig. 11. Horizontal profiles of the average velocity magnitude over a plane 1.5 m above ground level in different domain regions according to the lines in Fig. 8 and different grid resolutions: (a) $x = -370$ m, (b) $x = 300$ m, (c) $y = 50$ m, (d) $y = 340$ m.

the contour and line plots for grid G5. In summary, the convergence study suggested us that a grid with six refinement levels is fine enough to accurately resolve the wind velocity although the grid with five refinements captures the flow characteristics well as well.

4.3. Effects of turbulence model

In this section, we performed a sensitivity analysis of the solution to different turbulence models with a grid of six refinement levels. Fig. 12 shows the wind velocity field at pedestrian level (1.5 m above the local terrain) for three turbulence model, Spalart–Allmaras (panel a), realizable $k - \epsilon$ (panel b) and $k - g$ SST (panel c). Globally, the three turbulence models show the same velocity distribution structures

along the building with the same orders of magnitude. The presence of stagnation points (regions with zero velocity—dark blue areas in the contour plots) is more accentuated in the Spalart–Allmaras model. It is known that two-equation models like $k - \epsilon$ and $k - g$ SST have an anomalous behavior in stagnation points with unphysical overproduction of turbulent kinetic energy [52]. The flow detachment areas are characterized by similar separation lengths for the three models.

Velocity magnitudes extracted along the straight lines in Fig. 8 are plotted in Fig. 13 at a height of 1.5 m. The Figure quantitatively supports the fact that the three turbulence models show minimum differences in the velocity fields except for panel (a) where the $k - \epsilon$ underpredicts the velocity in the near-building region. In the final comparison with the other body-fitted software, we employed the $k - g$

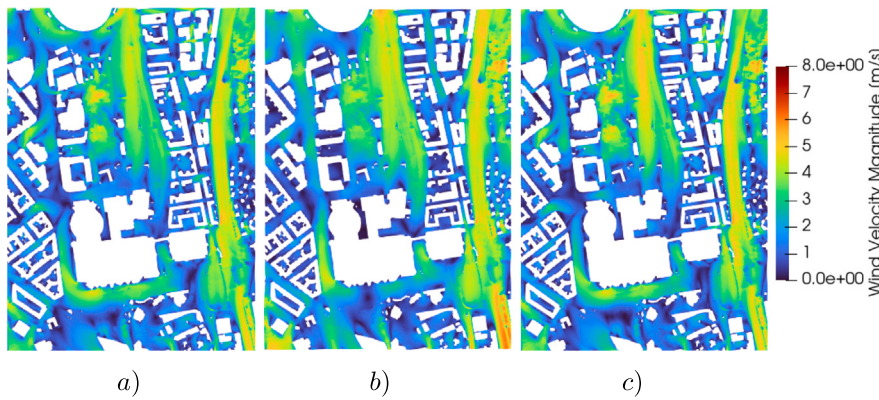


Fig. 12. Wind velocity magnitude over a plane 1.5 m above ground level using three different turbulence models: (a) Spalart–Allmaras, (b) $k - \epsilon$, (c) $k - g$ SST.

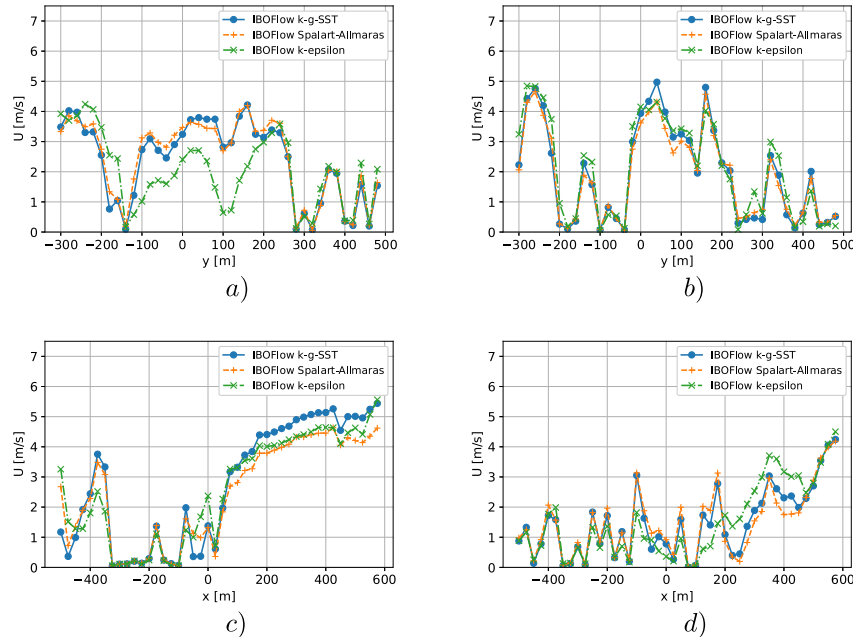


Fig. 13. Horizontal profiles of the average velocity magnitude over a plane 1.5 m above ground level in different domain regions according to the lines in Fig. 8 and using three different turbulence models: (a) $x = -370$ m, (b) $x = 300$ m, (c) $y = 50$ m, (d) $y = 340$ m.

SST model as the y_+ is high in the city and the $k - g$ SST model is more stable for coarser grids in the immersed boundary framework.

4.4. Comparison with body-fitted simulation software

In the following section we compare the simulation results using IBOFlow with two body-fitted solvers established for professional wind analysis in the built environment: Helyx and MISKAM.

4.4.1. Helyx

The numerical simulations have been carried out using Helyx v3.2 [53], a commercial CFD code based on the open-source OpenFOAM software platform. This setting represents state-of-art simulations using body-fitted mesh techniques for professional wind analysis in the building permit phase [12]. The set-up follows the requirements outlined in [16,54] and is in alignment with the previously described modeling approach. The main characteristics are given hereafter. The realizable $k - \epsilon$ closure turbulence model [36] is used. All the governing equations have been discretized with second-order schemes. The atmospheric wind boundary layer profiles set out in ESDU 01008 [55] have been used as inlet boundary conditions for the wind velocity vector and the turbulence quantities, following the description in Section 2.2.1.

The mesh settings and the wall functions used on the far field ground surface have been appropriately tuned in order to preserve the desired velocity and turbulent profiles up to the area of the CFD domain where the buildings have been explicitly modeled. A non-slip boundary condition has been used for all the ground surfaces and the modeled buildings. A slip wall condition has been chosen for the top and side surfaces. The mesh consists of roughly 25 million cells. Using local refinements, the maximum cell size near critical locations is 0.3 m. More than 10 cells are used over narrow passages and at least 4 prism layer cells are generated below the pedestrian height of 1.5 m.

4.4.2. MISKAM

MISKAM (Microscale Climate and Dispersion Model) is a three-dimensional non-hydrostatic numeric flow and dispersion model for small-scale estimations of wind behavior and pollutant concentrations, suitable for the evaluation of dense urban areas [56–58]. MISKAM requires information about the road network, three-dimensional buildings and local meteorological data. When air pollution is considered, the emission rate and source locations have to be specified [58]. MISKAM is limited by the fact that the domain cannot include the local topography; all buildings are placed on a flat ground plane. Usually this is a reasonable simplification for relatively flat urban areas and

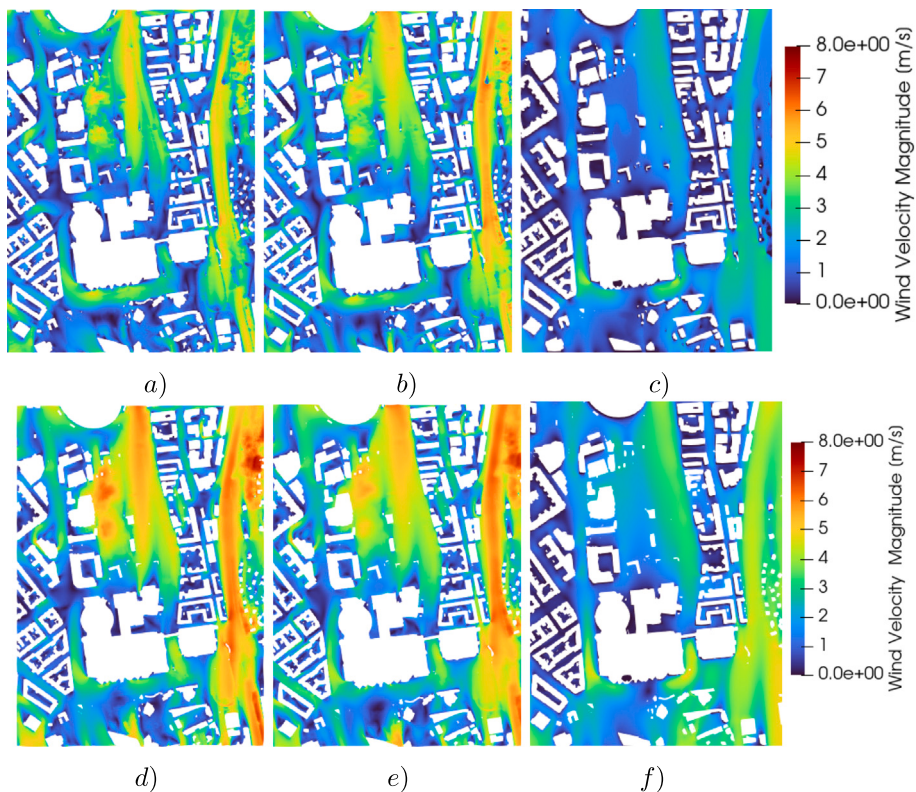


Fig. 14. Velocity over a plane 1.5 m (panel a–c) and 10 m (panel d–f) above ground level for simulation using (a) and (d) IBOFlow, (b) and (e) Helyx/OpenFoam, (c) Wind Velocity in the cell 0.9–2 m above the flat ground in MISKAM and (f) Wind Velocity in the cell 8–12 m above the flat ground in MISKAM.

commonly used commercially to save both computational and pre-processing time. In order to account for the hill on the north-east side of the domain, which as previously mentioned is expected to affect the local wind velocity, the geometrical feature has been included as a 3D body. The ground topography outside of the area of interest has not been considered. The grid is Cartesian and consists of 270 000 cells in the horizontal plane and a variable vertical resolution, where the cell height increases with elevation from 0.3 m at ground level up to 50 m. The total height is 484.5 m divided in 53 vertical levels. A standard turbulent $k - \epsilon$ model is used and a roughness length of 1 cm.

4.4.3. Comparison

Here, we will quantify and stress the need of properly accounting for the local terrain topography when simulating complex urban areas that are not flat. We will compare three numerical solvers, the body-fitted commercial software MISKAM that is limited to assume a flat ground everywhere, with Helyx/OpenFoam and IBOFlow that are capable to account for altitude differences. Note that differences in the general setup exist between the three solvers, most apparently in the turbulence model, yet all three simulation settings follow the BPGs. In Fig. 14 a comparison of (a) IBOFlow, (b) Helyx/OpenFoam and (c) MISKAM can be seen at two different heights, 1.5 m and 10 m above the local terrain level.

Comparing the three pedestrian level planes in Fig. 14 the wind velocity field, in general, shows, almost everywhere, similarities between the three solvers from a qualitative points of view, with a similar distribution of stagnation points and flow detachment regions. In particular, we observe a very good agreement between the simulations using IBOFlow (a) and Helyx (b) showcasing that a solver based on the immersed boundary method is very well suited for the simulation of complex urban terrain. Regarding the effects of the terrain, it immediately appears that the values of velocities in the flat terrain simulation (c) are smaller compared with the other two cases (a–b) where the local roughness is explicitly resolved. The flow structures in the central

region of the domain and in the right part close to the highway look very different with high velocities in panels (a) and (b) and low velocities in panel (c). These differences can be explained considering the local terrain topography by correlating the wind velocity with the elevation field shown in Fig. 8. The zones with the largest mismatches are characterized by the presence of hills in the central region (altitude 20 m), in the bottom part before the large building and in the right part of the domain (altitude 40 m). A marked hill effect is present in the area with higher wind velocities on the top of the local hills [59]. On the other hand the flow around the main building in the lower part of the panel is captured properly as the ground is reasonably flat.

In the 10 m above ground level plane (Fig. 14d–e), we observe the same similarities and differences between the three numerical approaches reported in the previous paragraph. Also, at a larger distance from the ground, the varying topography will generate higher velocities over the higher urban peaks as illustrated in the panels (d) and (e) compared to the flat case scenario (f).

A more quantitative comparisons is reported in Fig. 15 showing the magnitudes of the wind velocity along the lines defined in Fig. 8 at 1.5 m. All the panels show the same trends: the IBOFlow solution (blue curve) is in very good agreement with the simulation results from Helyx/OpenFoam, where the maximum deviation is 2.3 m/s very locally but on average follows within 0.3 m/s difference over all lines. The local rough topography is responsible for the differences between MISKAM and the other two softwares where MISKAM underpredicts the velocity when hills are present, with a maximum error almost twice as large at 3.9 m/s and average deviation of around 1 m/s, but is able to capture the overall flow behavior comprising of stagnation points, wind re-direction and speed-up due to the built environment.

In general, practitioners simulating wind comfort in urban areas often assume a flat terrain to save pre-processing and computational time. However, given the different results using two different terrain configuration, we recommend to resolve the local terrain topography for wind comfort simulations in an urban neighborhood when non-negligible elevation changes of the order of 20/40 m are present.

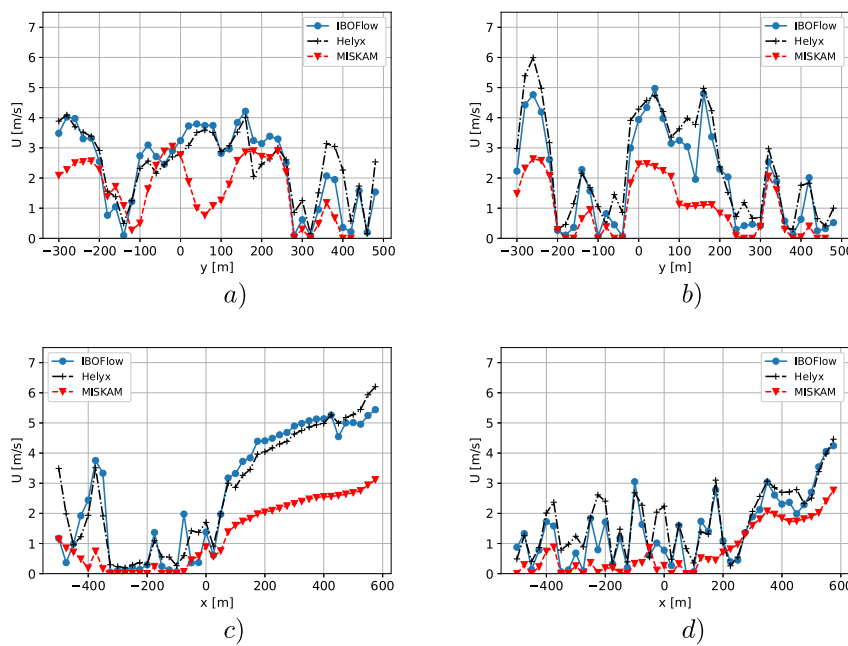


Fig. 15. Horizontal profiles of the average velocity magnitude over a plane 1.5 m above ground level in different domain regions according to the lines in Fig. 8 and using the three different numerical solvers: (a) $x = -370$ m, (b) $x = 300$ m, (c) $y = 50$ m, (d) $y = 340$ m.

5. Conclusions

In this study, an immersed boundary simulation approach using RANS equations has been validated against experiments in a wind tunnel and compared to two commercially used body-fitted softwares at urban scale for a complex topography neighborhood in Gothenburg, Sweden. The immersed boundary approach eliminates the complicated pre-processing of urban geometries by allowing for the automatic meshing of a Cartesian octree grid and making negligible the computational time spent for complex body-fitted mesh generation.

The wind tunnel scale validation features a grid resolution study and turbulence model comparison. The grid resolution study shows that the best practice guidelines for urban simulations, provided for body-fitted mesh and hexagonal prisms cells, can be safely applied also for an immersed-boundary numerical methodology. The same trend is suggested in the urban neighborhood simulations where the only grid that was giving lower velocity results was not satisfying the BPGs.

At the urban scale, it was shown that including the complex terrain is crucial in a complex urban topography to capture morphology-induced physical phenomena like hill effects when the terrain is characterized by differences in variations of the order of 20-40 m. In general, IBOFlow could provide a wind velocity field similar to a body-fitted code like Helyx/OpenFoam reducing almost to zero the pre-processing time for mesh generation and increasing the computational speed with a GPU parallelization.

It can be concluded that the immersed boundary methodology has shown a great potential to predict the urban microclimate while improving the cost of simulations significantly by eliminating the complicated pre-processing.

As future developments, the immersed boundary framework can be easily extended by coupling building energy models to simulate heat transfer, simulating pollutant dispersion and modeling the presence of vegetation or blue areas. Additionally, incorporating Large-Eddy Simulation LES is a potential future development, providing a more accurate representation of unsteady phenomena and further enhancing the predictive capabilities of the framework.

CRediT authorship contribution statement

Patricia Vanký: Writing – review & editing, Writing – original draft, Visualization, Validation, Methodology, Investigation, Data curation, Conceptualization. **Andreas Mark:** Writing – review & editing, Supervision, Software, Methodology, Conceptualization. **Franziska Hunger:** Writing – review & editing, Visualization, Validation, Software, Methodology, Investigation, Data curation, Conceptualization. **Gabriella Villamor Saucedo:** Software, Methodology. **Marie Haeger-Eugensson:** Software, Methodology, Conceptualization. **Jens Christian Bennetsen:** Software, Resources, Methodology. **Joaquim Tarraso:** Conceptualization. **Marco Adelfio:** Conceptualization. **Angela Sasic Kalagasisid:** Writing – review & editing, Supervision, Project administration, Investigation, Funding acquisition, Conceptualization. **Gaetano Sardina:** Writing – review & editing, Visualization, Validation, Supervision, Methodology, Investigation, Funding acquisition, Conceptualization.

Declaration of competing interest

The authors declare that they have no known competing financial interests or personal relationships that could have appeared to influence the work reported in this paper.

Data availability

Data will be made available on request.

Acknowledgments

This work was supported by the Swedish Research Council for Sustainable Development Formas under the grants 2019-01169 and 2019-01885. The computations were enabled by resources provided by the Swedish National Infrastructure for Computing (SNIC) at HPC2N partially funded by the Swedish Research Council through grant agreement no. 2018-05973. This work is also part of the Digital Twin Cities Centre supported by Sweden's Innovation Agency Vinnova under Grant No. 2019-00041.

Finally, we would like to thank some people for critical support during this work. Firstly, Professor Jan Carmeliet and his team at ETH for allowing the usage of experimental data for simulation validation purposes in this paper. More over, we thank Dag Wästberg, expert in wind analysis in practice, for his input on common commercial practice of wind analysis in urban planning.

References

- [1] World Urbanization Prospects: The 2018 Revision, Department of Economic and Social Affairs, Population Division, United Nations, 2018, online Edition.
- [2] G. Mills, Urban climatology: History, status and prospects, *Urban Clim.* 10 (2014) 479–489, <http://dx.doi.org/10.1016/j.ulclim.2014.06.004>.
- [3] K.C. Seto, B. Güneralp, L.R. Hutyra, Global forecasts of urban expansion to 2030 and direct impacts on biodiversity and carbon pools, *Proc. Natl. Acad. Sci.* 109 (40) (2012) 16083–16088, <http://dx.doi.org/10.1073/pnas.1211658109>.
- [4] B. Blocken, J. Carmeliet, Pedestrian wind environment around buildings: Literature review and practical examples, *J. Therm. Environ. Build. Sci.* 28 (2) (2004) 107–159, <http://dx.doi.org/10.1177/1097196304044396>.
- [5] B. Blocken, J. Carmeliet, Pedestrian wind conditions at outdoor platforms in a high-rise apartment building: generic sub-configuration validation, wind comfort assessment and uncertainty issues, *Wind Struct.* 11 (1) (2008) 51–70.
- [6] B. Blocken, W. Janssen, T. van Hooff, CFD simulation for pedestrian wind comfort and wind safety in urban areas: General decision framework and case study for the eindhoven university campus, *Environ. Model. Softw.* 30 (2012) 15–34, <http://dx.doi.org/10.1016/j.envsoft.2011.11.009>.
- [7] Y.-D. Huang, R.-W. Hou, Z.-Y. Liu, Y. Song, P.-Y. Cui, C.-N. Kim, et al., Effects of wind direction on the airflow and pollutant dispersion inside a long street canyon, *Aerosol. Air Qual. Res.* 19 (5) (2019) 1152–1171, <http://dx.doi.org/10.4209/aaqr.2018.09.0344>.
- [8] N. Antoniou, H. Montazeri, M. Neophytou, B. Blocken, CFD simulation of urban microclimate: Validation using high-resolution field measurements, *Sci. Total Environ.* 695 (2019) 133743, <http://dx.doi.org/10.1016/j.scitotenv.2019.133743>.
- [9] S. Valger, N. Fedorova, CFD methods in architecture and city planning, in: *Journal of Physics: Conference Series*, Vol. 1425, IOP Publishing, 2019, 012124.
- [10] J. Brozovsky, A. Simonsen, N. Gaitani, Validation of a CFD model for the evaluation of urban microclimate at high latitudes: A case study in Trondheim, Norway, *Build. Environ.* 205 (2021) 108–175, <http://dx.doi.org/10.1016/j.buildenv.2021.108175>.
- [11] W. Wang, H. Chen, L. Wang, S. Wang, Integrating multiple models into computational fluid dynamics for fine three-dimensional simulation of urban waterfront wind environments: A case study in Hangzhou, China, *Sustainable Cities Soc.* 85 (2022) 104088, <http://dx.doi.org/10.1016/j.scs.2022.104088>.
- [12] T.-O. Hägbo, K.E.T. Giljarhus, Sensitivity of urban morphology and the number of cfd simulated wind directions on pedestrian wind comfort and safety assessments, *Build. Environ.* (2024) 111310.
- [13] M. Langheinrich, K. Seifert, An advanced workflow for simulating high resolution wind fields over complex urban terrain including single tree objects, in: IGARSS 2019-2019 IEEE International Geoscience and Remote Sensing Symposium, IEEE, 2019, pp. 7657–7660.
- [14] T.-O. Hägbo, K.E.T. Giljarhus, B.H. Hjertager, Influence of geometry acquisition method on pedestrian wind simulations, *J. Wind Eng. Ind. Aerodyn.* 215 (2021) 104665, <http://dx.doi.org/10.1016/j.jweia.2021.104665>.
- [15] J. Franke, A. Hellsten, K. Schlünzen, B. Carissimo, Best practice guideline for the CFD simulation of flows in the urban environment-a summary, in: 11th Conference on Harmonisation Within Atmospheric Dispersion Modelling for Regulatory Purposes, Cambridge, UK, 2007, Cambridge Environmental Research Consultants, 2007.
- [16] Y. Tominaga, A. Mochida, R. Yoshie, H. Kataoka, T. Nozu, M. Yoshikawa, T. Shirasawa, AJI guidelines for practical applications of CFD to pedestrian wind environment around buildings, *J. Wind Eng. Ind. Aerodyn.* 96 (10–11) (2008) 1749–1761, <http://dx.doi.org/10.1016/j.jweia.2008.02.058>.
- [17] B. Blocken, Computational fluid dynamics for urban physics: Importance, scales, possibilities, limitations and ten tips and tricks towards accurate and reliable simulations, *Build. Environ.* 91 (2015) 219–245, <http://dx.doi.org/10.1016/j.buildenv.2015.02.015>.
- [18] B. Maronga, S. Banzhaf, C. Burmeister, T. Esch, R. Forkel, D. Fröhlich, V. Fuka, K.F. Gehrke, J. Geletić, S. Giersch, et al., Overview of the palm model system 6.0, *Geosci. Model Dev.* 13 (3) (2020) 1335–1372.
- [19] I. Suter, T. Grylls, B.S. Sütl, S.O. Owens, C.E. Wilson, M. van Reeuwijk, Udales 1.0: A large-eddy simulation model for urban environments, *Geosci. Model Dev.* 15 (13) (2022) 5309–5335.
- [20] S. Kaijima, R. Bouffanais, K. Willcox, S. Naidu, Computational fluid dynamics for architectural design, *Archit. Des.* 83 (2) (2013) 118–123, <http://dx.doi.org/10.1002/ad.1566>.
- [21] D. Kim, The Application of CFD To Building Analysis and Design: A Combined Approach of an Immersive Case Study and Wind Tunnel Testing (Ph.D. thesis), Virginia Tech, 2014.
- [22] C.S. Peskin, The immersed boundary method, *Acta Numer.* 11 (2002) 479–517, <http://dx.doi.org/10.1017/S0962492902000077>.
- [23] D.J. Wiersema, K.A. Lundquist, F.K. Chow, Mesoscale to microscale simulations over complex terrain with the immersed boundary method in the weather research and forecasting model, *Mon. Weather Rev.* 148 (2) (2020) 577–595, <http://dx.doi.org/10.1175/MWR-D-19-0071.1>.
- [24] F. Auguste, G. Réa, R. Paoli, C. Lac, V. Masson, D. Cariolle, Implementation of an immersed boundary method in the Meso-NH v5.2 model: applications to an idealized urban environment, *Geosci. Model Dev.* 12 (6) (2019) 2607–2633, <http://dx.doi.org/10.5194/gmd-12-2607-2019>.
- [25] F. Auguste, C. Lac, V. Masson, D. Cariolle, Large-eddy simulations with an immersed boundary method: pollutant dispersion over urban terrain, *Atmosphere* 11 (1) (2020) 113, <http://dx.doi.org/10.3390/atmos11010113>.
- [26] D. Muñoz-Esparza, J.A. Sauer, H.H. Shin, R. Sharman, B. Kosović, S. Meech, C. García-Sánchez, M. Steiner, J. Knievel, J. Pinto, et al., Inclusion of building-resolving capabilities into the fasteddy® GPU-LES model using an immersed body force method, *J. Adv. Modelling Earth Syst.* 12 (11) (2020) e2020MS002141, <http://dx.doi.org/10.1029/2020MS002141>.
- [27] G. Oh, M. Yang, J.-I. Choi, Large-eddy simulation-based wind and thermal comfort assessment in urban environments, *J. Wind Eng. Ind. Aerodyn.* 246 (2024) 105682.
- [28] S. Jafari, N. Chokani, R.S. Abhari, Terrain effects on wind flow: Simulations with an immersed boundary method, in: *Turbo Expo: Power for Land, Sea, and Air*, Vol. 54617, 2011, pp. 869–878.
- [29] J. Allegrini, A wind tunnel study on three-dimensional buoyant flows in street canyons with different roof shapes and building lengths, *Build. Environ.* 143 (2018) 71–88, <http://dx.doi.org/10.1016/j.buildenv.2018.06.056>.
- [30] A. Mark, R. Rundqvist, F. Edelvik, Comparison between different immersed boundary conditions for simulation of complex fluid flows, *Fluid Dyn. Mater. Process.* 7 (3) (2011) 241–258.
- [31] J. Van Doormaal, G. Raithby, Enhancements of the SIMPLE method for predicting incompressible fluid flows, *Numer. Heat Transfer* 7 (2) (1984) 147, <http://dx.doi.org/10.1080/01495728408961817>.
- [32] C. Rhie, W.L. Chow, Numerical study of the turbulent flow past an airfoil with trailing edge separation, *AIAA J.* 21 (11) (1983) 1525, <http://dx.doi.org/10.2514/3.8284>.
- [33] A. Mark, B.G. van Wachem, Derivation and validation of a novel implicit second-order accurate immersed boundary method, *J. Comput. Phys.* 227 (13) (2008) 6660–6680, <http://dx.doi.org/10.1016/j.jcp.2008.03.031>.
- [34] S. Allmaras, F. Johnson, P. Spalart, Modifications and non-linear in the boundary layer. several validation cases clarifications for the implementation of the Spalart-Allmaras in both two and three dimensions were provided, exhibit- turbulence model, in: *Seventh International Conference on Computational Fluid Dynamics, ICCFD7*.
- [35] S. Pope, *Turbulent Flows*, Cambridge University Press, 2000.
- [36] T.-H. Shih, W. Liou, A. Shabbir, Z. Yang, J. Zhu, A new $k - \epsilon$ eddy viscosity model for high Reynolds number turbulent flows, *J. Comput. Phys.* 24 (3) (1995) 227–238.
- [37] F.R. Menter, Two-equation eddy-viscosity turbulence models for engineering applications, *AIAA J.* 32 (8).
- [38] F.R. Menter, M. Kuntz, M.R. Langtry, Ten years of industrial experience with the SST turbulence model, *Turb. Heat Mass Transfer* 4.
- [39] D. Wilcox, *Turbulence Modeling for CFD*, DCW Industries, 2010.
- [40] G. Kalitzin, G. Medic, G. Iaccarino, P. Durbin, Near-wall behavior of RANS turbulence models and implications for wall functions, *J. Comput. Phys.* 204, <http://dx.doi.org/10.1016/j.jcp.2004.10.018>.
- [41] P. Richards, R. Hoxey, Appropriate boundary conditions for computational wind engineering models using the $k - \epsilon$ turbulence model, *J. Wind Eng. Ind. Aerodyn.* 46 (1993) 145–153, [http://dx.doi.org/10.1016/0167-6105\(93\)90124-7](http://dx.doi.org/10.1016/0167-6105(93)90124-7).
- [42] J. Wieringa, Updating the davenport roughness classification, *J. Wind Eng. Ind. Aerodyn.* 41 (1–3) (1992) 357–368, [http://dx.doi.org/10.1016/0167-6105\(92\)90434-C](http://dx.doi.org/10.1016/0167-6105(92)90434-C).
- [43] D.B. Spalding, et al., A single formula for the law of the wall, *J. Appl. Mech.* 28 (3) (1961) 455–458.
- [44] B. Aupoix, P. Spalart, Extensions of the spalart-allmaras turbulence model to account for wall roughness, *Int. J. Heat Fluid Flow* 24 (4) (2003) 454–462, [http://dx.doi.org/10.1016/S0142-727X\(03\)00043-2](http://dx.doi.org/10.1016/S0142-727X(03)00043-2).
- [45] B. Aupoix, Roughness corrections for the $k - \omega$ shear stress transport model: Status and proposals, *J. Fluids Eng.* 137 (2) <http://dx.doi.org/10.1115/1.4028122>.
- [46] F. Chedevergne, Analytical wall function including roughness corrections, *Int. J. Heat Fluid Flow* 73 (2018) 258–269, <http://dx.doi.org/10.1016/j.ijheatfluidflow.2018.08.001>.
- [47] A.G. Davenport, Rationale for determining design wind velocities, *J. Struct. Div.* 86 (5) (1960) 39–68.
- [48] B. Blocken, T. Stathopoulos, J. Carmeliet, CFD simulation of the atmospheric boundary layer: wall function problems, *Atmos. Environ.* 41 (2) (2007) 238–252, <http://dx.doi.org/10.1016/j.atmosenv.2006.08.019>.
- [49] Lantmäteriet, Lantmäteriet, 2022, URL <https://www.lantmateriet.se/>.
- [50] A. Logg, V. Naserentin, D. Wästerberg, O. Eleutheriou, A. Olsson, A. Annlöv, Dtcc Builder, 2022, URL <https://gitlab.com/dtcc-platform/dtcc-builder>.

- [51] V. Naserentin, A. Logg, Digital twins for city simulation: Automatic, efficient, and robust mesh generation for large-scale city modeling and simulation, arXiv preprint arXiv:2210.05250 doi:10.48550/arXiv.2210.05250.
- [52] P.A. Durbin, On the $k-\epsilon$ stagnation point anomaly, Int. J. Heat Fluid Flow 17 (1996) 9–90.
- [53] engys, Helyx-os, 2024, URL <https://engys.com/products/helyx>.
- [54] C. Corporation, Wind microclimate guidelines for developments in the city of London, 2019, pp. 1–15.
- [55] ESDU, Computer program for wind speeds and turbulence properties: flat or hilly sites in terrain with roughness changes, 2024, URL https://www.esdu.com/cgi-bin/ps.pl?t=doc&p=esdu_01008c.
- [56] J. Eichhorn, Entwicklung Und Anwendung Eines Dreidimensionalen Mikroskaligen Stadtklima-Modells (Ph.D. thesis), 1989.
- [57] J. Eichhorn, Validation of a microscale pollution dispersal model, in: Air Pollution Modeling and Its Application XI, Springer, 1996, pp. 539–547.
- [58] J. Eichhorn, A. Kniffka, The numerical flow model MISKAM: State of development and evaluation of the basic version, Meteorol. Z. (2010) 81–90, <http://dx.doi.org/10.1127/0941-2948/2010/0425>.
- [59] B. Blocken, A. van der Hout, J. Dekker, O. Weiler, Cfd simulation of wind flow over natural complex terrain: Case study with validation by field measurements for Ria De Ferrol, Galicia, Spain, J. Wind Eng. Ind. Aerodyn. 147 (2015) 43–57.